



Hybrid Nanocomposites of Hydroxyapatite, Eu_2O_3 , Graphene Oxide Via Ultrasonic Power: Microstructure, Morphology Design and Antibacterial for Biomedical Applications

M. K. Ahmed^{1,2} · Nasser S. Awwad³ · Hala A. Ibrahim^{4,5} · M. Afifi⁶

Received: 10 November 2021 / Accepted: 26 February 2022 / Published online: 26 March 2022
© The Author(s), under exclusive licence to Springer Science+Business Media, LLC, part of Springer Nature 2022

Abstract

Post-implantation infections are regarded as a major issue in the biomedical field. Further, many investigations are continuous towards developing antibacterial biocompatible materials. In this regard, hydroxyapatite (HAP), erbium oxide (Eu_2O_3), and graphene oxide (GO) were introduced in nanocomposites combinations, including single, dual, and triple constituents. The nanoparticles of HAP, Eu_2O_3 , and nanosheets of GO are synthesized separately, while dispersed in the nanocomposites simultaneously. The morphological investigation showed that HAP was configured in a rod-like shape while the nano ellipsoidal shape of Eu_2O_3 was confirmed. The particle size of the ternary nanocomposite containing HAP/ Eu_2O_3 /GO reached the length of 40 nm for the rods of HAP and around 28 nm for the length axis of ellipsoidal Eu_2O_3 nanoparticles. The roughness average increased to be about 54.7 nm for HAP/GO and decreased to 37.9 nm for the ternary nanocomposite. Furthermore, the maximum valley depth (R_v) increased from HAP to the ternary nanocomposite from 188.9 to 189.8 nm. Moreover, the antibacterial activity was measured, whereas the inhibition zone of HAP/ Eu_2O_3 /GO reached 13.2 ± 1.1 mm for *Escherichia coli* and 11.4 ± 0.8 mm for *Staphylococcus aureus*. The cell viability of the human osteoblast cell lines was evaluated to be $98.5 \pm 3\%$ for the ternary composition from $96.8 \pm 4\%$ for the pure HAP. The existence of antibacterial activity without showing cytotoxicity against mammalian cells indicates the compatibility of nanocomposites with biomedical applications.

Keywords Hydroxyapatite · Eu_2O_3 · Graphene oxide · Antibacterial · Cell viability

1 Introduction

Nowadays, antibiotic-resistant germs or superbugs problem is considered public health problem [1]. The bacteria do not resist one drug, instead, they become multi-drug resistant (MDR), which requires a new generation of drugs based on non-biotic anti-bacterial materials [2]. Many nanomaterials have anti-bacterial properties, besides entering the cell easily due to their nano size [3]. However, hydroxyapatite (HAP) is one of the apatite families distinguished by the OH group [4, 5]. Its high biocompatibility properties come from its similarity with the inorganic phase in bones [6, 7]. Many studies investigated the behavior of HAP for tissue and bone engineering, drug delivery system, protein separation, and orthopedics [8]. HAP exhibits two crystallographic orientations, which are hexagonal and monoclinic; the hexagonal phase transforms to the monoclinic crystalline phase at approximately 200 °C [9]. Further, HAP shows high osteoconductivity, bioactivity, non-toxicity, and non-inflammatory properties [10]. Nevertheless, the calcium phosphate

✉ M. K. Ahmed
m.khalaf@sci.suezuni.edu.eg

¹ Faculty of Nanotechnology for Postgraduate Studies, Cairo University, El-Sheikh Zayed 12588, Egypt

² Department of Physics, Faculty of Science, Suez University, Suez 43518, Egypt

³ Chemistry Department, Faculty of Science, King Khalid University, P.O. Box 9004, Abha 61413, Saudi Arabia

⁴ Biology Department, Faculty of Science, King Khalid University, P.O. Box 9004, Abha 61413, Saudi Arabia

⁵ Department of Semi Pilot Plant, Nuclear Materials Authority, P.O. Box 530, El Maadi, Egypt

⁶ Ultrasonic Laboratory, National Institute of Standards, Giza, Egypt

component has high popularity in biomaterial applications. They have not been studied for tissue regeneration and antibacterial treatments, but even for anti-cancer therapy [11]. One of the advantages of HAP is the numerous methods that could be used for its preparation. The co-precipitation method has been utilized in the large-scale production of HAP. The synthesis conditions have an essential effect on the physicochemical properties of the obtained compositions [12]. The main problem in pure HAP is the low mechanical properties and low toughness resistance compared with the natural bone tissues, which limit its applications in high load-bearing [13]. The desired properties of HAP can be reached in two ways, maintaining the HAP crystal structure and replacing Ca^{2+} , PO_4^{3-} or OH^- with other dopant atoms. On the other hand, using nanocomposites containing HAP which could be done by combining HAP with other phases to introduce a wide range of multifunctionality, including high thermal stability, good antibacterial behavior, besides mechanical properties [14]. It is reported that nanocomposite materials can introduce the desired multi-functionality property [15]. The adequate nanocomposite material could gain high mechanical by a reinforcing material without decreasing its bioactivity [13].

Further, improving the optical properties of nanocomposite containing HAP to be used in bio-imaging is an example of the gathered properties which can occur via the nanocomposite configuration. Moreover, erbium oxide (Eu_2O_3) is one of the rare earth composites which has been studied in smart drug delivery, photothermal therapy, and bioimaging [14]. Erbium is suggested to be used in the field of cell imaging due to its photoluminescent properties and its ability to target and bind to the cell surface and reach receptor-mediated endocytosis [16]. Moreover, Eu_2O_3 has sharp emission peaks which are very fluorescent, hence reinforcing using it in bio-imaging. In addition, Eu_2O_3 exhibits anti-bacterial properties against most strains of bacteria, therefore it could give good results in cell proliferation and anti-bacterial test with HAP as a composite configuration [17]. Cell imaging is very important to detect disease in clinical application, especially with the long lifetime of Eu_2O_3 radiation which is around 9.7 ms [18]. However, with the high biocompatibility of HAP with the anti-bacterial and optical properties of Eu_2O_3 a good nanocomposite can be resulted for use in a wide range of medical applications.

Furthermore, for the mechanical properties weakness of HAP and to promote the antibacterial activity, the graphene oxide (GO) can be suggested to be incorporated as the ternary phase. GO is the oxygenated form of the monolayer graphene sheet, which is structured in packed two-dimensional carbon atoms. GO introduces an extremely large surface area which makes it chemically active besides its biocompatibility, biostability, and mechanical properties by allowing the stress to be transferred in the composite

more easily with enhancing the interfacial bonding [19, 20]. Besides, the two-dimensional structure of GO can fill the pores, which prevents crack growth, therefore reinforcing the HAP structure [21]. For those properties, GO was studied to be used for biosensors, and cellular imaging usages [22]. The large surface area of GO nanosheets enlarges its loading capacity and encourages its drug delivery utilizations. Moreover, it was reported that GO could improve the bioactivity of materials such as gelatin [23]. Few studies estimated using graphene for scaffolds fabrication in tissue engineering [24]. The incorporation of GO in HAP might develop the bioactivity and mechanical properties, besides the proliferation and adhesion of osteoblasts [25]. Akhavan et al. reported the antibacterial activity of GO against *Escherichia coli* and *Staphylococcus aureus* [26]. Kattle et al. showed that Eu_2O_3 is non-toxic up to 0.5 mM [18]. Moreover, Zunil et al. showed that $\text{Eu}_2\text{O}_3/\text{GO}$ composite improved GO optical properties to be used widely from electronic material to optoelectronic material [27]. In addition, Yingqi Li et al. showed that Eu_2O_3 less than 1.0 mg/mL and less than 600 nm in diameter could penetrate the cell without causing damage [28]. Moreover, the dispersibility degree of nanoparticles plays a vital role in the Physico-chemical properties of the nanocomposite. For instance, the electrical conductivity depends strongly on the mean free path of charge carriers, which can be enlarged significantly if the electron can move from its conduction band to the graphene surface. The Eu_2O_3 possesses a low band (3.66 eV), allowing its electrons to be generated via incident photons. The excellent contact between Eu_2O_3 nanoparticles and GO nanosheets might support the generated electrons from the former to the latter surface. The jumping process might reduce the combined probability of formed charge carriers [7, 29]. The excellent dispersibility of the formed nanocomposites can be done via different techniques, including magnetic stirrer and ultrasonic power [30]. The probe sonicator is considered a fast and powerful tool to exfoliate graphite layers to be converted to graphene nanosheets [31]. Thus, the probe sonicator can exfoliate GO nanosheets and encapsulate HAP or Eu_2O_3 through the former nanosheets like sandwich configuration.

The previous literature shows that HAP is suggested to be used in different biomedical applications, while its low mechanical and antibacterial properties are major problems. The mechanical properties can be solved by considering HAP as a matrix and reinforcing it with nanosheets of GO. Therefore, the mechanical properties can be enhanced and the crack growth can be inhibited. The nanoparticles of Eu_2O_3 addition can enhance the antibacterial properties of HAP due to the releasing of Eu^{3+} ions and Eu_2O_3 nanoparticles which can easily penetrate the bacterial cell wall and cause damage to DNA. Moreover, that antibacterial mechanism has been detected by Sivaselvam et al. they

reported FESEM micrographs to show MgO nanoparticles penetrate the cell wall of bacteria [32]. Furthermore, that can be reached by designing a nanocomposite containing HAP/Eu₂O₃ as a matrix and reinforced by nanosheets of GO.

The combinations of the binary nanocomposite of HAP/GO, and HAP/Eu₂O₃ and the ternary nanocomposite of HAP/Eu₂O₃/GO. The objective is to improve the antibacterial properties of HAP and maintain its biocompatibility if not improved. The used compositions are based on several previous studies, but it was rare to find a complete study focusing on the physio-chemical influences based on the gathering of HAP/Eu₂O₃/GO. Previous studies such as Li et al. used GO as filler in the HAP matrix to obtain HAP/GO nanocomposite by electrophoretic nanotechnology to be used as a coating material for biomedical applications. They reported that cell viability enhanced towards L929 and MG63 cell lines [20]. Further, Ramadas et al. prepared a nanocomposite of HAP/GO, HAP was prepared using a hydrothermal method, and GO was synthesized by Hummer's method. They found that the addition of GO enhanced the biocompatibility of HAP toward A431 cells [33]. Moreover, Xiong et al. prepared a nanocomposite of HAP/GO/sodium alginate (SA). They found that the addition of GO improved the compressive strength to be around 3 MPa and the compressive modulus reached 0.254 MPa [34]. In addition, the previous studies of using Eu₂O₃ in biomedical applications. Consequently, the individual components were suggested and it was expected that the combination between them enhanced the biological response and improved the antibacterial properties without damaging the mammalian cells.

That work aims to investigate nanocomposites of HAP, GO at different combinations that will be prepared via ultrasonication power. The structural and morphological of nanocomposites will be investigated, besides the physical and chemical characterization, and the response of nanocomposites against bacteria and toward human cells in vitro.

2 Materials and Methods

2.1 Inorganic Precursors

Calcium chloride dihydrate [CaCl₂·2H₂O], diammonium hydrogen phosphate [(NH₄)₂HPO₄], europium oxide (Eu₂O₃), potassium permanganate [KMnO₄], graphite, hydrochloric acid [HCl], were purchased from LOBA, ODISHA, India, and they were utilized without further purifications.

2.2 Synthesis Procedure

2.2.1 HAP Synthesis

The co-precipitation method has been employed to prepare HAP as follows. CaCl₂·2H₂O (0.5 M) was added to a beaker and (NH₄)₂HPO₄ (0.3 M) was added to another beaker, deionized water (100 mL) was then added to each beaker creating a calcium and phosphate solution, respectively. The phosphate solution was then added slowly to the calcium solution; diluted ammonia was used to maintain a pH of 11 ± 0.1. That resulted mixture was stirred for 2 h using a magnetic stirrer at 1200 rpm. The solution was then allowed to settle for a day to allow precipitation, resulting in a precipitated gel. The precipitated gel was then washed by deionized water and filtered several times; it was then dried at a temperature of 50–60 °C in a furnace. HAP was then collected from the furnace as powder.

2.2.2 GO Synthesis

The modified hummers method has been employed to prepare GO as described before [35]. Graphite was produced from a natural source, Hassawi rice biomass waste from Al-Ahsa governorate at eastern Saudi Arabia region. Briefly, 0.5 g of graphite were added to 120 mL of H₂SO₄ then mixed thoroughly. A weight of KMnO₄ (12 g) was then added to the mixture and was then stirred for 2 h using a magnetic stirrer at 800 rpm. Then, 300 mL of deionized water was added slowly to the mixture at a rate of ~ 10 mL/h. After cooling the mixture, 10 mL of H₂O₂ have been dropped on the mixture and stirred with high power for 30 min. The mixture was then filtered and then in using a probe sonicator, it was dispersed in 500 mL HCL (20 wt%) for 15 min. The mixture was then dried at a temperature of 50–60 °C in a furnace.

2.2.3 Nanocomposites

Five compositions were then obtained as follows: (1) 1 g of HAP, (2) 1 g of Eu₂O₃, (3) 1 g of HAP/1 g of Eu₂O₃, (4) 1 g of HAP/0.05 g GO, and (5) 1 g of HAP/1 g of Eu₂O₃/0.05 g of GO. The nanocomposites were then dispersed separately in tubes containing 50 mL of deionized water to be suspended via *ultrasonic probe sonicator* for 15 min. To collect the powder samples, the tubes were then centrifuged at 6000 rpm for 10 min. The collected powders were then dried for several hours at 50–60 °C.

2.3 XRD Measurements

On an X-ray diffractometer (analytical-x 'pertpro, Cu K α1 radiation, λ = 1.5404 Å, 45 kV, 40 mA, Netherlands), X-ray

diffraction (XRD) pattern was estimated. The samples were prepared by grinding them separately using a mortar for amounts around 10 g. Then the powder is put in a sample holder using a spatula. After that, by using a smooth piece of glass the sample holder was filled. Finally, the sample of glass was removed.

2.4 FTIR Measurements

The transmittance FTIR analysis was done with a (Perkin-Elmer 2000) spectrometer in the range of 400–4000 cm^{-1} . The preparation stages were done as follows:

1. obtaining around 2 g of the powder.
2. The sample was mixed in a mortar with KBr with a ratio of 20:1.
3. The sample is placed in a holder and compressed hard for adhering to the sample perfectly.
4. The sample is put in the instrument then the software is activated from 400 to 4000 cm^{-1} .

2.5 XPS Measurements

The obtained powder samples were studied using the XPS instrument of (PerkinElmer PHI 5600). The scanning range was up to 1400 eV with a resolution of 0.1 eV.

2.6 FESEM

A scanning electron microscope (FESEM, model: QUANTA-FEG250, Netherlands) is utilized to detect surface morphology and roughness. The obtained SEM images were introduced into Gwyddion 2.4 software for 3D roughness images and roughness parameters.

2.7 In Vitro Cell Viability Tests

The human osteoblasts cell line was cultured in Dulbecco's modified Eagle's medium (DMEM, Gibco) at 37 °C and 5% CO_2 to measure the cell viability ratio. Around 5 mg of each sample was added into a 96 well plate to be serialized. The density of cells was around of 5×10^3 cells/ cm^2 . After three incubation days, the medium was removed, and MTT (3-(4,5-dimethylthiazol-2-yl)-2,5-diphenyltetrazolium bromide) was injected into each well, after which the cell viability was detected via an optical analyzer. Cell viability was calculated as [36–38]:

$$\text{Viability(\%)} = \frac{\text{Mean optical density of test samples}}{\text{Mean optical density of the control}} \times 100$$

(1)

The statistical analysis was done using Medcalc software version 15.0 (Mariakerke and Belgium). Further, the continuous variables were represented as mean standard deviation (SD) (\pm).

2.8 Antibacterial Activity

The antibacterial activity was tested via the diffusion disk technique. It was done against (*Staphylococcus aureus* = *S. aureus*), which was obtained from ATCC Number 29213, and (*Escherichia coli* = *E. coli*), which was obtained from American Type Culture Collection (ATCC) number 25922. The initial concentration of the powdered samples was around 20 mg/mL. The inhibition zone was measured in mm after 24 h of exposure. The experiment has been repeated three times to evaluate the standard deviation values.

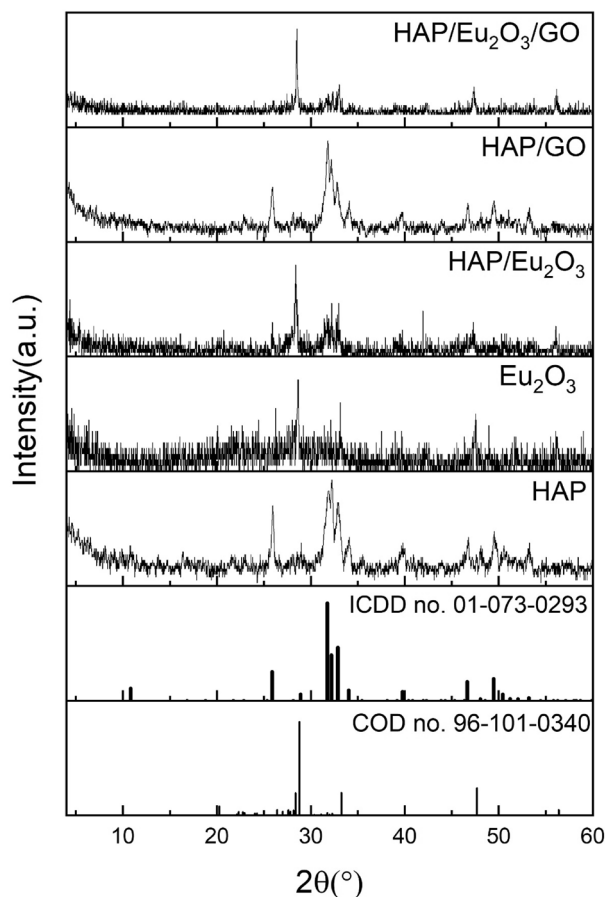


Fig. 1 XRD patterns of HAP, Eu_2O_3 , HAP/ Eu_2O_3 , HAP/GO, and HAP/ Eu_2O_3 /GO nanocomposites, besides HAP and Eu_2O_3 upon no. 01-073-0293 and 96-101-0340

3 Results and Discussion

3.1 XRD

In Fig. 1, the XRD measurements of all compositions. HAP seems to be formed in a hexagonal structure upon the ICDD card no.01-073-0293. Further, the phase of Eu_2O_3 was formed in a cubic symmetry according to the ICDD card no. 96-101-0340. The essential peaks of GO tend to be very low due to the irregularity of its structure in 3-dimensions which caused in the destruction of its crystallographic order [20]. XRD shows the final ternary nanocomposites of HAP/ Eu_2O_3 /GO as separate phases. The crystallinity of HAP seems to be lower than the Eu_2O_3 phase, which is assigned to the difference in preparation conditions between HAP and Eu_2O_3 . While HAP was prepared without exposure to high temperatures, Eu_2O_3 was annealed at 450 °C for hours. The crystal growth is promoted via the annealing process. The crystallinity of all compositions are computed from the following relation [5]:

$$X_c\% = \frac{\sum A_C}{\sum A_C + \sum A_A} \times 100$$

where X_c is the crystallinity, A_c and A_A are the all area under crystalline peaks and all areas under amorphous peaks, respectively.

The crystallinity of as-prepared HAP is 76%, while Eu_2O_3 is 89%. The nanocomposite of HAP and Eu_2O_3 reveals a crystallinity of 71%, which matches with the previous reports that Eu_2O_3 could cause a deterioration of HAP's crystallinity [39]. Adding HAP with GO enlarges the crystallinity to be around 67%. It seems as GO inhibits the HAP crystal to grow, although the XRD pattern does not differ much from the pure HAP pattern. Whatever the final composition of HAP/ Eu_2O_3 /GO shows crystallinity around 76%.

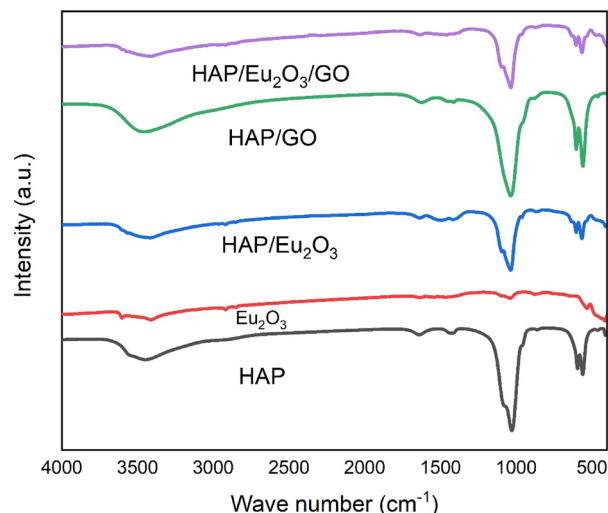


Fig. 2 FTIR spectra of HAP, Eu_2O_3 , HAP/ Eu_2O_3 , HAP/GO and HAP/ Eu_2O_3 /GO nanocomposites

The crystallite size is computed from Scherrer's equation [40]:

$$L = \frac{K\lambda}{\beta \cos\theta}$$

L is the crystallite size, λ is the wavelength of the X-ray source, β is FWHM intensity, K is the shape factor, and θ is Bragg's angle. Besides all angles are converted into radian.

The prepared HAP shows crystallite size around 12 nm and Eu_2O_3 crystallites around 23 nm, while the composition of HAP/ Eu_2O_3 has crystallite size around 21 nm. The HAP/GO is the smallest crystallite size which was around 16 nm and the final composition HAP/ Eu_2O_3 /GO, the crystallite size was around 10 nm which indicates the contribution of GO to inhibit the growth of the crystals.

Table 1 FTIR transmittance infrared bands of the different nanocomposites of HAP, Eu_2O_3 and GO

HAP	Eu_2O_3	HAP/ Eu_2O_3	HAP/GO	HAP/ Eu_2O_3 /GO	Assignment	Ref.
413	413	410	–	404	Bending mode of PO_4^{3-}	[43]
475	–	–	472	471	Vibrational mode of O–P–O	[44]
566	532	566	564	566	Bending mode of O–P–O	[5]
604	–	603	605	603	Bending mode of O–P–O	[45]
873	878	867	874	872	Vibrational mode of CO_3^{2-}	[46]
965	–	963	963	–	PO_4^{3-} stretching	[47]
1034	1039	1035	1035	1034	Anti-symmetric stretch of CO_3^{3-}	[48]
1096	–	1093	1093	1094	P–O stretching	[49]
1426	–	1417	1415	–	Vibrational mode of CO_3^{2-}	[50]
1454	1467	1493	1456	1463	Vibrational mode of CO_3^{2-}	[47, 50]
1635	1644	1639	1643	1635	Absorbed water	[47]
2913	2918	2919	2925	2919	C–H vibrations	[46, 50]
3435	3410	3415	3432	3413	O–H vibrations	[51, 52]

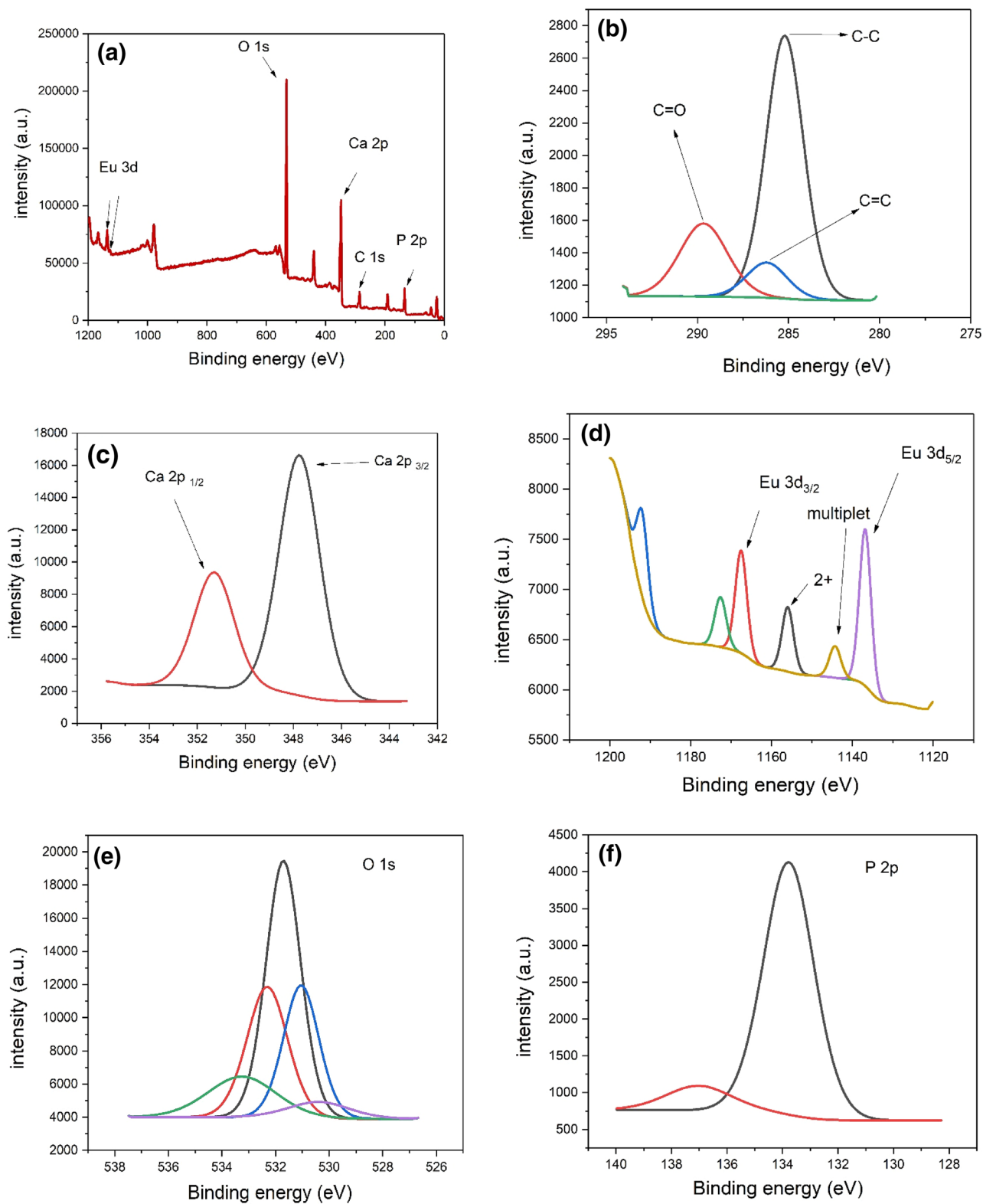


Fig. 3 XPS of HAP/Eu₂O₃/GO for wide range, **(b–f)** C 1s, Ca 2p, Eu 3d, O 1s and P2p, respectively

3.2 FTIR Spectra

Fourier-transform infrared analysis was performed to confirm the presence of the vibrational groups, as illustrated in Fig. 2. The detected bands at 475, 604, and 965 cm^{-1} belong to the phosphate group as reported in Table 1, confirming the main bands of apatite composition [41]. The bands at 1635, 3435 cm^{-1} are assigned to the O–H bond, which ensures the hydroxyl group, confirming the HAP formation in four compositions [5]. In addition, the band at 566 cm^{-1} is attributed to the HPO_4^{2-} vibrational group [39]. It can be reported that the band at 3570 cm^{-1} belongs to the vibrational stretching mode of OH^- , while the band at 633 cm^{-1} refers to the arising of the librational stretching mode [12]. The band of 1420 cm^{-1} can be ascribed to the carbonated groups through the HAP structure. The presence of carbonate group with HAP structure due to its affinity to absorb carbon from the ambient atmosphere [5]. The detected peak at 873 cm^{-1} is supposed to be at 833 cm^{-1} while it is shifted due to an interaction between COO^- and Ca^{2+} [13].

In the di-nanocomposite of HAP/GO, there is an increase in the intensity of bands around 1000–1600 cm^{-1} due presence of C=O around 1643 cm^{-1} and C–O around 1094 cm^{-1} . Further, those bands can not detect easily because of the existence of HAP [42]. However, the analysis confirms HAP and GO compositions.

3.3 XPS

The X-ray photoelectron spectroscopy (XPS) spectrum of the ternary composition is illustrated in Fig. 3. In Fig. 3a, there are two peaks with different intensities, at 1125 and 1135 eV can represent the oxidation states +2 and +3 of Eu 3d, respectively [9, 52]. They indicate that the contribution of Eu(III) is much more than Eu(II). In other words, the ratio between Eu^{3+} and Eu^{2+} is very high. The peaks at 131, 284, 348, 543, and 1135 eV belong to P 2p, C 1s, Ca 2p, O 1s, Eu 3d, confirming the ternary nanocomposite of HAP/ Eu_2O_3 /GO as the previous studies [10, 52]. Figure 3b shows C 1s spectrum with 3 peaks. The peak at 285 eV belongs to –C–C–, which determines the bonds between carbon atoms, while the second peak at 289 eV is assigned to –C=O determines the oxygenated carbon. Therefore, both peaks might describe GO structure. Further, the third peak at 286 eV belongs to C=C could describe the edges of the graphene structure, which must make a double bond with another oxygen or a double bond with carbon to complete the structure [53, 54]. That could explain why C–C is the highest peak, while C=O C=C is the lower peak. In addition, those carbon bonds could belong to the hydroxyapatite due to its affinity to absorb carbon from the air [52]. Furthermore, the binding energy of 285 eV belongs to C 1s, which is ascribed to C–H and C–C bonds, while the peak at 531 eV belongs to

OH^- ions [55]. The peaks at 131 eV and 348 eV belong to phosphate and calcium ions. Those peaks describe the full oxidation states of P^{5+} and Ca^{2+} [52]. However, XPS analysis confirms the existence of all elements in all compositions. Figure 3c shows the binding energy of Ca 2p, the peak at 347 eV belongs to the angular momentum of 3/2, and the peak at 351 eV belongs to the angular momentum of 1/2 [10, 42]. In Fig. 3d; the two large peaks at 1136 eV belong to Eu 3d with angular momentum 5/2 and at 1167 eV belongs to Eu 3d with angular momentum 3/2, which are a result of the spin–orbit coupling. Besides, those peaks belong to the Eu(III) state, and it is reported that peaks at 1155 eV and 1144 eV belong to Eu^{2+} oxidation state and multiple states, respectively [56]. Figure 3e, f shows O 1s and P 2p spectrum where 531.1 eV belongs to O–Ca while 531.6 for O–H and 532,133 eV for O=P and phosphate 2p [9, 52].

3.4 Morphology

Figure 4a shows SEM micrograph that contains information about the size and shape of the as-prepared HAP. It is obvious that HAP has been demonstrated in nanorod structures with aggregated particles. The diameter of nanorods is about 40 nm, while the length varies to 120 nm. As seen in Fig. 4b, the morphology Eu_2O_3 tends to be porous with small ellipsoidal particles accumulated together with a size around 28 nm. In Fig. 4c, the composition of HAP/ Eu_2O_3 is shown, and the morphology of HAP is changed slightly. It seems like less agglomeration with fewer diameters around 30 nm and smaller in length to be about 80 nm with spherical particles between the rods with 70 nm of diameter belonging to the Eu_2O_3 phase. The composition of HAP/GO is shown in Fig. 4d and the tendency to agglomerate with dimensions of 30 nm. Whatever the final structure of HAP/ Eu_2O_3 /GO is displayed in Fig. 4e shows ellipsoidal and nanorod particles with dimensions about 20 nm. A porous structure is formed which can induce the proliferation process by transporting the nutrient and oxygen to inside the osteoblasts cells [29].

The roughness behavior is shown in Fig. 5a–e, and the roughness parameters are shown in Table 2. The highest roughness of HAP/GO composition with roughness average (R_a) of 54.7 nm and the maximum height of the roughness (R_t) of 478 nm. The increasing of roughness could be ascribed to the collapsing of the 2D structure of GO in the three-dimension. Therefore, lowering the crystallinity induces more defects and more disorders. The progression of roughness still in the nano-scale range helps in developing the adsorption of proteins. Besides, increasing roughness could increase the cell attachment by interlocking the biomaterial with the biological cell [57]. In contrast with the composition of Eu_2O_3 which shows good crystallinity and finer particles, that morphology leads to the least rough behavior with R_a around 35 nm and R_t around 318 nm, and

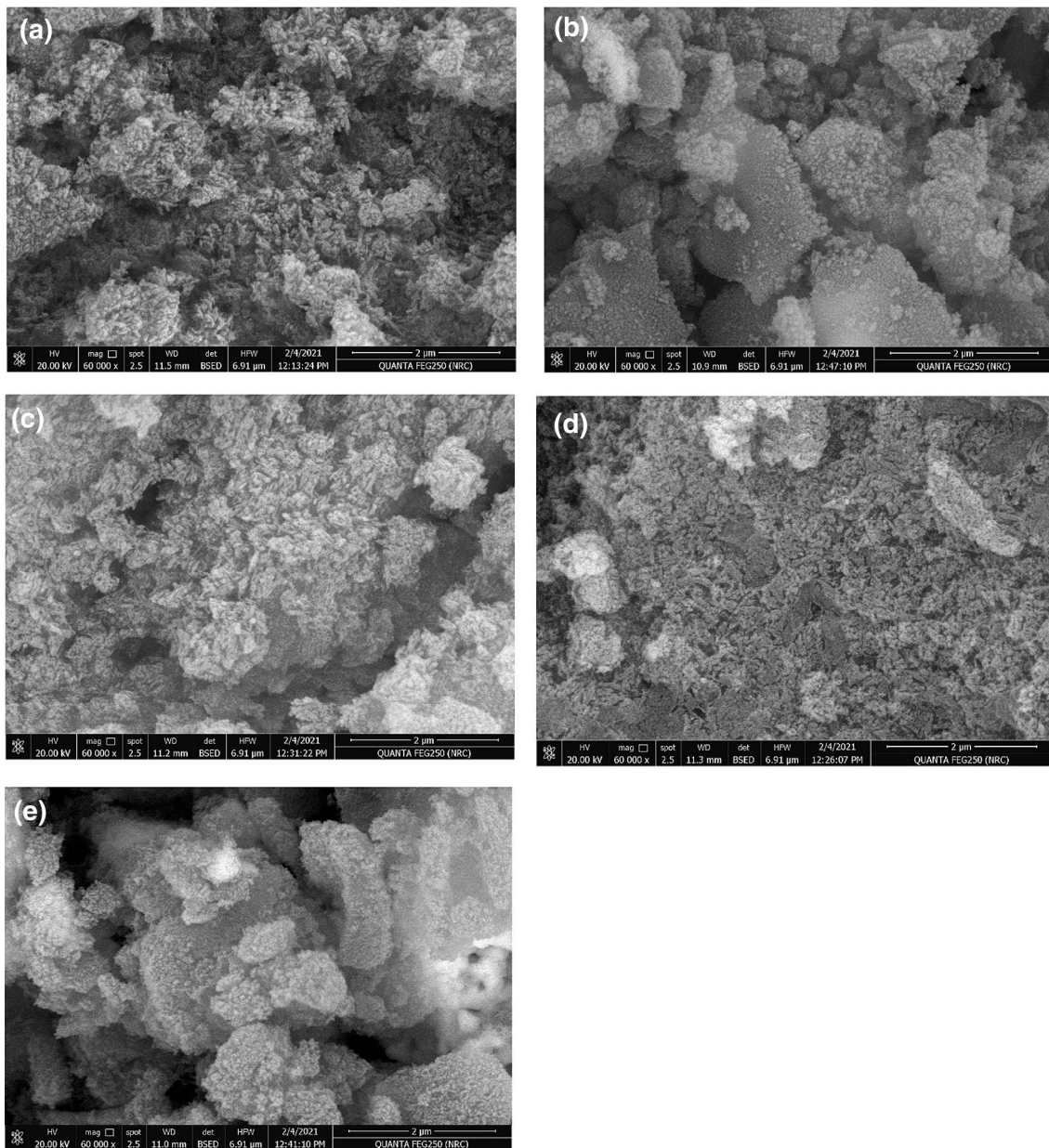


Fig. 4 FESEM micrographs of the different nanocomposites, where **a** HAP, **b** Eu_2O_3 , **c** HAP/ Eu_2O_3 di-nanocomposite **d** HAP/GO di-nanocomposite, and **e** HAP/ Eu_2O_3 /GO ternary-nanocomposites

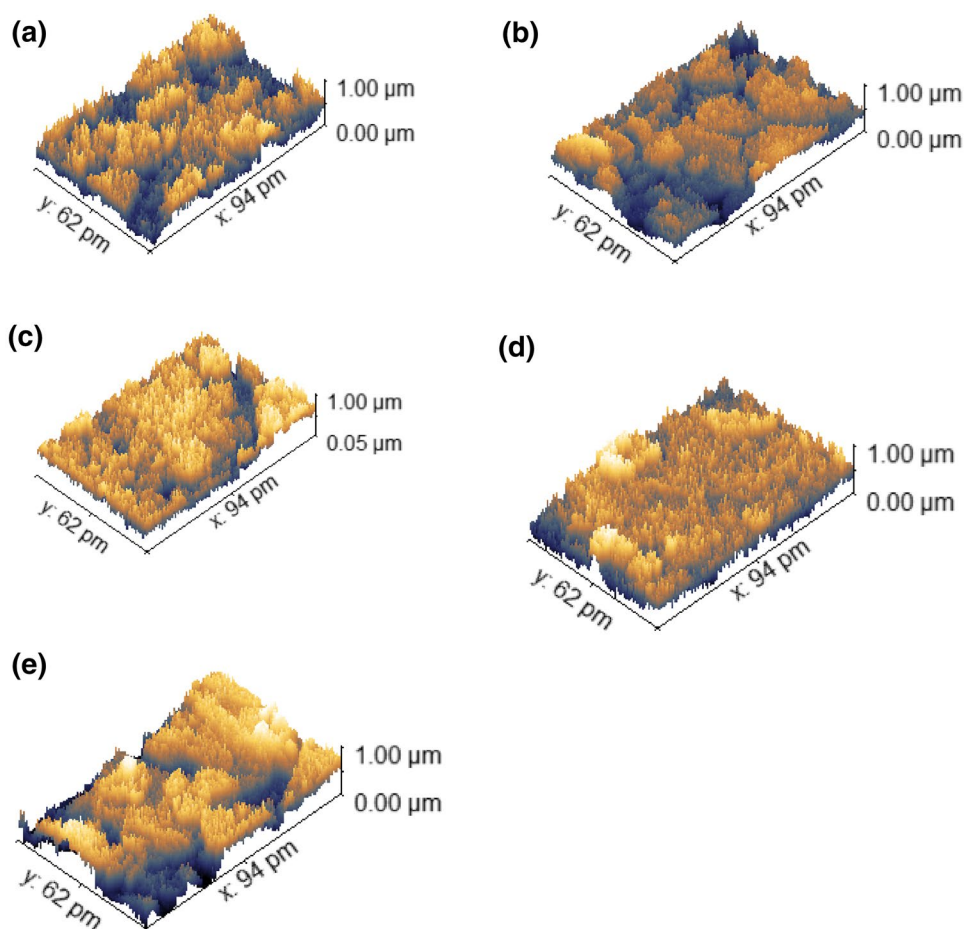
it is reported that the proliferation of osteoblast increases with decreasing roughness [58]. In addition, the decrease in roughness can affect the corrosion rate, therefore the lifetime of the biomaterial [59].

3.5 Microstructural Features

The TEM micrographs in Fig. 6a show the pure HAP composition. It is noticed the nanorod shape with a diameter of about 20 nm and length about 50 nm. Further, the nanorods

are agglomerated in different places, which match with SEM micrographs. Figure 6b shows the composition of HAP/ Eu_2O_3 , which demonstrates the nanorods of HAP with a diameter around 20 nm and 70 nm in length and ellipsoidal particles of Eu_2O_3 with 15 nm in diameter, with an aspect ratio of 3.0. The ternary composition of HAP/ Eu_2O_3 /GO is shown in Fig. 6c, which exhibits dense particles with different shapes as like-rod, ellipsoidal, and sheets of graphene oxide. The average diameters of nanorods are around 8 nm, while the average diameter of ellipsoidal particles is around

Fig. 5 The roughness behavior obtained from FESEM micrographs, where **a** HAP, **b** Eu_2O_3 , **c** HAP/ Eu_2O_3 , **d** HAP/GO and **e** HAP/ Eu_2O_3 /GO nanocomposites, respectively



13 nm which agrees well with SEM micrographs and Scherrer's equation.

It could be reported that the morphological features of hydroxyapatite depend strongly on the formation mechanism of HAP's crystals. It can be hypothesized that HAP does not crystallize in one step, rather, it grows through intermediate stages, depending on the pH value of the medium [60, 61]. In detail, at high pH values, the calcium and phosphate ions are gathering in the amorphous calcium phosphate phase, which might transform to di-calcium phosphate di-hydrate (DCPD), to octa-calcium phosphate (OCP), which is transitioned to HAP crystals [60, 61]. However, at low pH values, the OCP might come before DCDP. These scenarios are suggested to occur at room temperature. It could be noticed that

controlling the preparation conditions can manipulate the desired morphology of synthesized HAP, which is essential for interactions with surroundings.

Herein, it might be noticed that the materials of HAP, Eu_2O_3 , and GO have been mixed together in a physical reaction through a water medium. This physical reaction could be considered as an up-down process, whereas the starting nanoparticles were crushed under the stress of sonication. Further, this might allow the nanoparticles to be smaller, and in some probability, the crystals could grow. Moreover, the fragmented nanoparticles were able to permeate each other. Furthermore, the probe sonicator is powerful enough to exfoliate graphite multi-sheets to be in one-layer (graphene) nanosheets, although in this

Table 2 The roughness parameters of all compositions where R_a , R_q , R_t , R_v , R_p , and R_{tm} are roughness average, root mean square roughness, the maximum height of the roughness, maximum roughness valley depth, maximum roughness peak height, and the average maximum height of the roughness respectively

Composition	R_a (nm)	R_q (nm)	R_t (nm)	R_v (nm)	R_p (nm)	R_{tm} (nm)
HAP	45.7	59.1	437.8	188.9	248.8	349.2
Eu_2O_3	35	45	318.4	171.9	146.4	267.1
HAP/ Eu_2O_3	51.6	66	426.9	217.2	209.7	363.4
HAP/GO	54.7	68.6	478	233.4	244.6	391.5
HAP/ Eu_2O_3 /GO	37.9	48	339.6	189.8	149.8	285

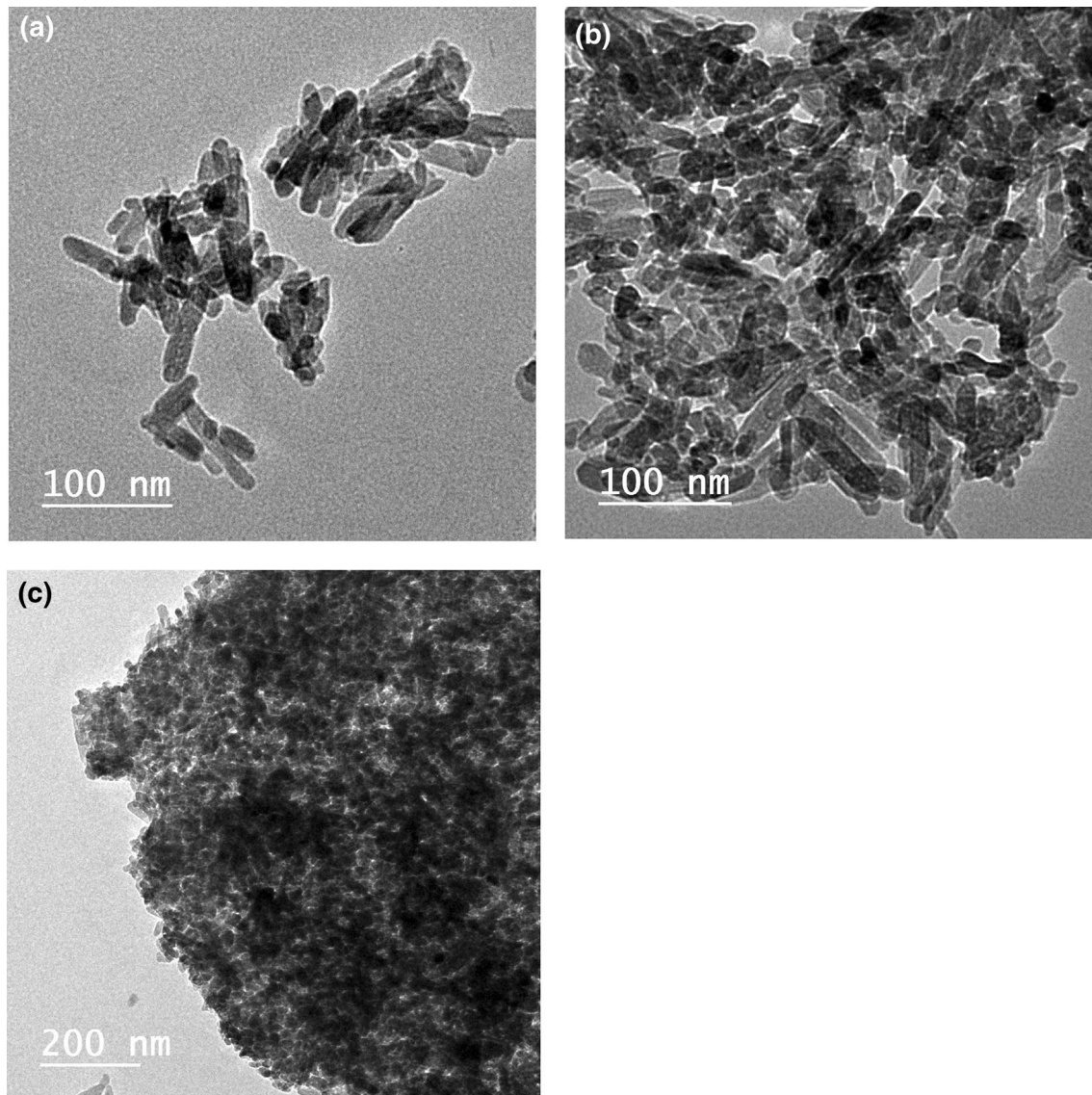


Fig. 6 TEM micrographs of **a** HAP nanorods, **b** HAP/Eu₂O₃ di-nanocomposite and **c** HAP/Eu₂O₃/GO ternary-nanocomposite

case, graphene oxide was used as a starting material from the beginning. Further, it could be reported that Sompech et al. clarified that the sonicator affects the particle size and can decrease the particle size significantly [62]. Also, it could be suggested that the graphene oxide nanosheets can act as a barrier to disturb the recrystallization of the surrounding molecules. Thus, the physical procedure to obtain these nanocomposites might re-construct the particle shape/size distribution via high powerful sonication.

3.6 EDX

EDX (Energy-Dispersive x-ray spectroscopy) analysis was performed to confirm HAP/Eu₂O₃/GO composite formation. The analysis is shown in Fig. 7 shows the existence

of C, O, P, Ca, and Eu with 25.95, 46.09, 10.87, 12.15, and 4.49%. The atomic weight percent of the contributions are listed in Table 2. It could be seen that the Ca/P ratio is around 1.45, which is relatively close to the empirical value of HAP components. Further, the presence of Eu is relatively high. Obviously, the oxygen element has a high atomic percent in the composite due to its sharing in all of the individual components as C–O and Eu–O, and O–H and is detected at 0.5 keV [63] (Table 3).

3.7 Cell Viability

Figure 8 demonstrates the cell viability of human osteoblast cell lines for 3 days with different compositions. HAP composition shows high cell viability of about 96.8%. It is

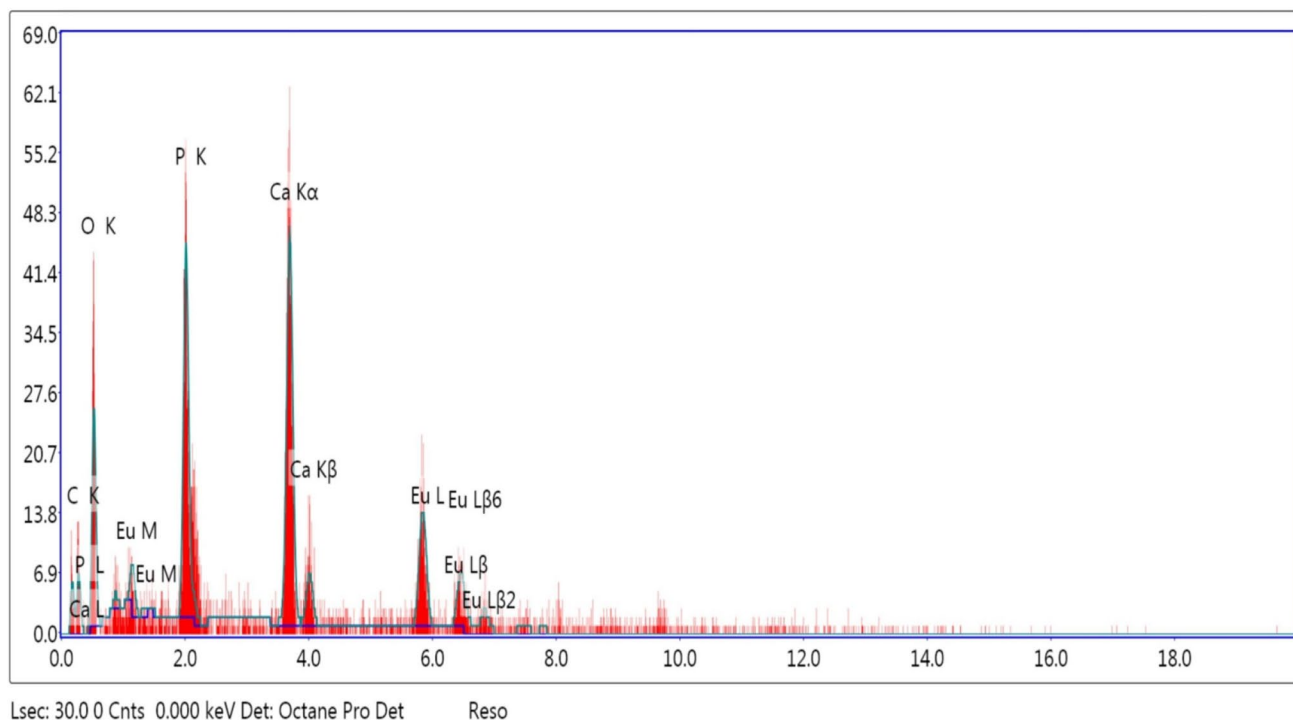


Fig. 7 EDX analysis of HAP/Eu₂O₃/GO nanocomposite which shows the chemical components of the ternary-nanocomposite

known that HAP is non-toxic and similar to the mineral bone structure; therefore, high cell viability results are expected. Eu₂O₃ is biocompatible and bioactive, which indicates its proliferation properties; however, the cell viability of the component is around 95.2%. by composing HAP and Eu₂O₃ the viability increases to 97.8%, while HAP/GO composition shows cell viability around 94.6%. It is reported that HAP composition has higher cell viability than HAP/GO except at GO/HAP [20]. The maximum cellular ability is observed at the ternary composition of HAP/Eu₂O₃/GO due to the biocompatibility of each component. The cell viability reached 98.5%, which indicates the compatibility of the components together as a nanocomposite biomaterial.

Table 3 The data of EDX analysis of the nanocomposite of HAP/Eu₂O₃/GO

Element	Weight %	Atomic %
C K	11.88	25.95
O K	28.11	46.09
P K	12.83	10.87
Ca K	18.56	12.15
Eu L	28.61	4.94

3.8 Anti-bacterial Activity

The antibacterial effect was investigated by measuring the inhibition zone on *E. coli* and *S. aureus* with the compositions after 24 h, and the results are revealed in Fig. 9. The anti-microbial tests help open the doors for using nanocomposites as drug delivery, an excellent solution for antibiotic resistance [17]. The pure HAP has no antibacterial effect against *E. coli* or *S. aureus* after 24 h, that does not mean there are no antibacterial properties at the composition. However, pure Eu₂O₃ exhibits an inhibition zone around 9.3 ± 0.9 mm for *E. coli* and 8.9 ± 0.9 mm for *S. aureus*. The effect on the two strains is due to the anti-microbial properties of Eu₂O₃ nanoparticles against all the bacterial strains [17]. The composition of HAP/Eu₂O₃ shows an inhibition zone of 10.2 ± 0.5 and 10.1 ± 1.1 mm for *E. coli* and *S. aureus* respectively. The inhibition zone of HAP/GO is around 11.3 ± 0.9 and 10.5 ± 0.9 mm for *E. coli* and *S. aureus* respectively. It is reported that the anti-bacterial effect of GO sheets is higher than the small ones [64]. In the ternary nanocomposite, the GO phase has sharp edges, which increase the ability to penetrate the cell membrane of the different species of bacteria [53]. In addition, the high anti-bacterial effect can be explained via the oxidation of lipids which can be induced by the oxidative nature of GO [65]. The antibacterial potency increases with Eu₂O₃ contribution due to the releasing of Eu³⁺ through the pathogenic media, whereas bacterial walls possess a high affinity

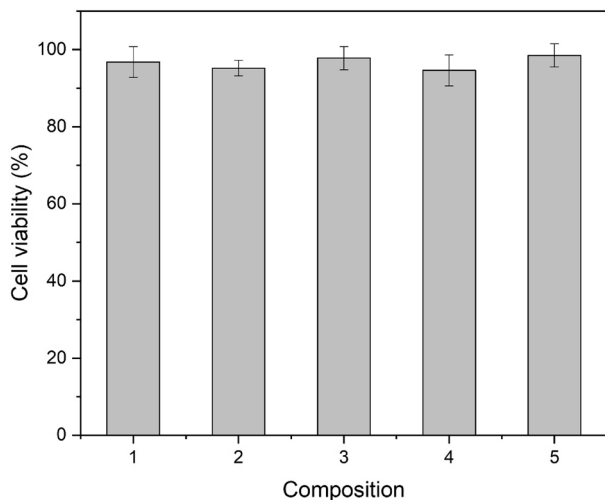


Fig. 8 The cell viability with composition of (1) HAP, (2) Eu_2O_3 , (3) HAP/ Eu_2O_3 , (4) HAP/GO and (5) HAP/ Eu_2O_3 /GO respectively toward human osteoblast cell line in vitro

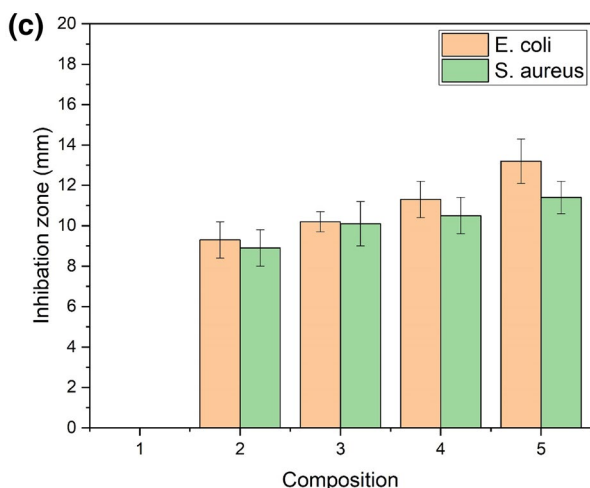
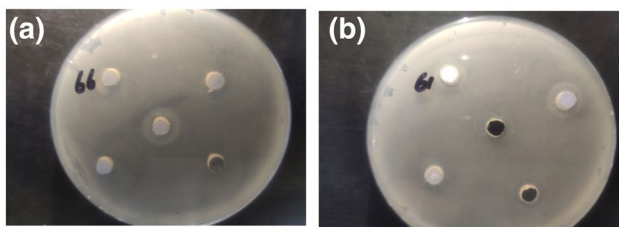


Fig. 9 The anti-bacterial behavior with the composition of HAP, Eu_2O_3 , HAP/ Eu_2O_3 , HAP/GO and HAP/ Eu_2O_3 /GO respectively against *E. coli* and *S. aureus*

towards these cations. In addition, the increasing of cations through the media provokes the formation of reactive

oxygen species (ROS) including OH^- and $\text{O}_2^{\cdot-}$ besides the oxyanions belong to GO. Further, the dissolved Eu might inhibit the original physiological function to work [17]. The ternary nano-composition shows the highest inhibition zone by 13.2 ± 1.1 mm for *E. coli* and 11.4 ± 0.8 mm for *S. aureus*, which is ascribed to the ability of anti-bacterial effect of the components individually with different mechanisms.

4 Conclusion

Different nanocomposites based on combinations of HAP, Eu_2O_3 , and GO were fabricated. The ternary nanocomposite of HAP/ Eu_2O_3 /GO has been developed in particle size around 20 nm and has a smoother surface than the pure HAP. The average roughness developed to be around 37.9 nm for the HAP/ Eu_2O_3 /GO composite. XRD analysis showed that the crystallinity of the ternary composite was around 76%. The cell viability of the composite reached 98.5% whereas, the inhibition zone of the HAP/ Eu_2O_3 /GO composite increased to 13.2 ± 1.1 mm for *E. coli* and 11.4 ± 0.8 mm for *S. aureus*, which can be considered as a development in biocompatibility for nanocomposites based on HAP.

Acknowledgements The authors appreciate the Deputyship for Research and Innovation, Ministry of Education in Saudi Arabia for funding this research work through the project number : IFP-KKU-2020/11.

Declarations

Conflict of interest The authors have not disclosed any competing interests.

References

1. R.S. Ambekar, B. Kandasubramanian, Advancements in nanofibers for wound dressing: a review. *Eur. Polym. J.* **117**, 304–336 (2019)
2. M.F.H.A. El-Kader, M.K. Ahmed, M.T. Elabbasy, M. Afifi, A.A. Menazea, Morphological, ultrasonic mechanical and biological properties of hydroxyapatite layers deposited by pulsed laser deposition on alumina substrates. *Surf. Coat. Technol.* **409**, 126861 (2021). <https://doi.org/10.1016/j.surfcoat.2021.126861>
3. V. Ponnillavan, S. Vasanthavel, R.K. Singh, S. Kannan, Influence of La^{3+} additions on the phase behaviour and antibacterial properties of ZrO_2 - SiO_2 binary oxides. *Ceram. Int.* **41**, 7632–7639 (2015)
4. N.H. de Leeuw, Local ordering of hydroxy groups in hydroxyapatite. *Chem Commun* (2001). <https://doi.org/10.1039/b104850n>
5. O. Kaygili, C. Tatar, F. Yakuphanoglu, S. Keser, Nano-crystalline aluminum-containing hydroxyapatite based bioceramics: synthesis and characterization. *J. Sol-Gel. Sci. Technol.* **65**, 105–111 (2012)

6. L. Wang, H. He, Y. Yu, L. Sun, S. Liu, C. Zhang et al., Morphology-dependent bactericidal activities of Ag/CeO₂ catalysts against *Escherichia coli*. *J. Inorg. Biochem.* **135**, 45–53 (2014)
7. M.K. Ahmed, S.F. Mansour, R. Al-Wafi, M. Afifi, V. Uskokovic, Gold as a dopant in selenium-containing carbonated hydroxyapatite fillers of nanofibrous epsilon-polycaprolactone scaffolds for tissue engineering. *Int. J. Pharm.* **577**, 118950 (2020)
8. F. Mohandes, M. Salavati-Niasari, In vitro comparative study of pure hydroxyapatite nanorods and novel polyethylene glycol/graphene oxide/hydroxyapatite nanocomposite. *J. Nanopart. Res.* (2014). <https://doi.org/10.1007/s11051-014-2604-y>
9. L.A. Zavala-Sanchez, G.A. Hirata, E. Novitskaya, K. Karandikar, M. Herrera, O.A. Graeve, Distribution of Eu(2+) and Eu(3+) ions in hydroxyapatite: a cathodoluminescence and raman study. *ACS Biomater. Sci. Eng.* **1**, 1306–1313 (2015)
10. S.-L. Iconaru, M. Motelica-Heino, D. Predoi, Study on Europium-doped hydroxyapatite nanoparticles by fourier transform infrared spectroscopy and their antimicrobial properties. *J. Spectrosc.* (2013). <https://doi.org/10.1155/2013/284285>
11. V. Uskokovic, M.A. Iyer, V.M. Wu, One ion to rule them all: combined antibacterial, osteoinductive and anticancer properties of selenite-incorporated hydroxyapatite. *J. Mater. Chem. B* **5**, 1430–1445 (2017)
12. C. Popa, C. Ciobanu, S. Iconaru, M. Stan, A. Dinischiotu, C. Negri et al., Systematic investigation and in vitro biocompatibility studies on mesoporous europium doped hydroxyapatite. *Open Chem.* **12**, 1032–1046 (2014)
13. M.G. Raucchi, D. Giugliano, A. Longo, S. Zepetelli, G. Carotenuto, L. Ambrosio, Comparative facile methods for preparing graphene oxide-hydroxyapatite for bone tissue engineering. *J. Tissue Eng. Regen. Med.* **11**, 2204–2216 (2017)
14. T.A.R.M. Lima, M.E.G. Valerio, X-ray absorption fine structure spectroscopy and photoluminescence study of multifunctional europium (III)-doped hydroxyapatite in the presence of cationic surfactant medium. *J. Lumin.* **201**, 70–76 (2018)
15. J.R. Vail, D.L. Burris, W.G. Sawyer, Multifunctionality of single-walled carbon nanotube–polytetrafluoroethylene nanocomposites. *Wear* **267**, 619–624 (2009)
16. T. Kataoka, S. Abe, M. Tagaya, Surface-engineered design of efficient luminescent europium(III) complex-based hydroxyapatite nanocrystals for rapid hela cancer cell imaging. *ACS Appl. Mater. Interfaces* **11**, 8915–8927 (2019)
17. S. Chaudhary, P. Sharma, S. Kumar, S.A. Alex, R. Kumar, S.K. Mehta et al., A comparative multi-assay approach to study the toxicity behaviour of Eu₂O₃ nanoparticles. *J. Mol. Liq.* **269**, 783–795 (2018)
18. K. Kattel, J.Y. Park, W. Xu, H.G. Kim, E.J. Lee, B.A. Bony et al., Water-soluble ultrasmall Eu₂O₃ nanoparticles as a fluorescent imaging agent: In vitro and in vivo studies. *Colloids Surf. A* **394**, 85–91 (2012)
19. S. Stankovich, D.A. Dikin, G.H. Dommett, K.M. Kohlhaas, E.J. Zimney, E.A. Stach et al., Graphene-based composite materials. *Nature* **442**, 282–286 (2006)
20. M. Li, Q. Liu, Z. Jia, X. Xu, Y. Cheng, Y. Zheng et al., Graphene oxide/hydroxyapatite composite coatings fabricated by electrophoretic nanotechnology for biological applications. *Carbon* **67**, 185–197 (2014)
21. H. Nosrati, R.S. Mamoory, D.Q.S. Le, C.E. Bünger, Preparation of reduced graphene oxide/hydroxyapatite nanocomposite and evaluation of graphene sheets/hydroxyapatite interface. *Diamond Related Mater.* **100**, 107561 (2019)
22. L. Feng, Y. Chen, J. Ren, X. Qu, A graphene functionalized electrochemical aptasensor for selective label-free detection of cancer cells. *Biomaterials* **32**, 2930–2937 (2011)
23. C. Wan, M. Frydrych, B. Chen, Strong and bioactive gelatin–graphene oxide nanocomposites. *Soft Matter* **7**, 6159 (2011)
24. J.H. Lee, Y.C. Shin, S.M. Lee, O.S. Jin, S.H. Kang, S.W. Hong et al., Enhanced osteogenesis by reduced graphene oxide/hydroxyapatite nanocomposites. *Sci. Rep.* **5**, 18833 (2015)
25. D. Lahiri, A.P. Benaduce, L. Kos, A. Agarwal, Quantification of carbon nanotube induced adhesion of osteoblast on hydroxyapatite using nano-scratch technique. *Nanotechnology* **22**, 355703 (2011)
26. M. Afifi, M.K. Ahmed, H.A. Ibrahim, N.S. Awwad, E. Abdel-Fattah, M.Y. Alshahrani, Improvement of physicochemical properties of ternary nanocomposites based on hydroxyapatite/CuO/graphene oxide for biomedical usages. *Ceram. Int.* **48**(3), 3993–4004 (2022). <https://doi.org/10.1016/j.ceramint.2021.10.186>
27. Z. Mo, Y. Zhao, R. Guo, P. Liu, T. Xie, Preparation and characterization of graphene/europium oxide composites. *Mater. Manuf. Processes* **27**, 494–498 (2011)
28. Y. Li, Z. Li, X. Zhou, P. Yang, Detection of nano Eu₂O₃ in cells and study of its biological effects. *Nano Biomed. Eng.* (2010). <https://doi.org/10.5101/nbe.v2i1.p24-30>
29. M.K. Ahmed, R. Ramadan, M. Afifi, A.A. Menazea, Au-doped carbonated hydroxyapatite sputtered on alumina scaffolds via pulsed laser deposition for biomedical applications. *J. Market. Res.* **9**, 8854–8866 (2020)
30. M.K. Ahmed, M. Afifi, M.S. Mostafa, A.F. El-kott, H.A. Ibrahim, N.S. Awwad, Crystal structure optimization, ultrasonic properties and morphology of Mg/Se co-dopant into annealed hydroxyapatite for biomedical applications. *J. Mater. Res.* (2021). <https://doi.org/10.1557/s43578-021-00148-y>
31. Z. Liu, J. Tian, C. Yu, Q. Fan, X. Liu, K. Yang et al., Ultrasonic fabrication of SO₄²⁻-doped g-C₃N₄/Ag₃PO₄ composite applied for effective removal of dyestuffs and antibiotics. *Mater. Chem. Phys.* **240**, 122206 (2020)
32. S. Sivaselvam, P. Premasudha, C. Viswanathan, N. Ponpandian, Enhanced removal of emerging pharmaceutical contaminant ciprofloxacin and pathogen inactivation using morphologically tuned MgO nanostructures. *J. Environ. Chem. Eng.* **8**, 104256 (2020)
33. M. Ramadas, G. Bharath, N. Ponpandian, A.M. Ballamurugan, Investigation on biophysical properties of hydroxyapatite/graphene oxide (HAp/GO) based binary nanocomposite for biomedical applications. *Mater. Chem. Phys.* **199**, 179–184 (2017)
34. G. Xiong, H. Luo, G. Zuo, K. Ren, Y. Wan, Novel porous graphene oxide and hydroxyapatite nanosheets-reinforced sodium alginate hybrid nanocomposites for medical applications. *Mater. Charact.* **107**, 419–425 (2015)
35. M.K. Ahmed, M.E. El-Naggar, A. Aldalbahi, M.H. El-Newehy, A.A. Menazea, Methylene blue degradation under visible light of metallic nanoparticles scattered into graphene oxide using laser ablation technique in aqueous solutions. *J. Mol. Liq.* **315**, 113794 (2020)
36. S.F. Mansour, S.I. El-dek, M. Ismail, M.K. Ahmed, Structure and cell viability of Pd substituted hydroxyapatite nano particles. *Biomed. Phys. Eng. Express* **4**, 045008 (2018)
37. M.F. Abdelbar, H.S. El-Sheshtawy, K.R. Shouier, I. El-Mehasseb, M. Ebeid E-Zeiny, M. El-Kemary, Halogen bond triggered aggregation induced emission in an iodinated cyanine dye for ultra sensitive detection of Ag nanoparticles in tap water and agricultural wastewater. *RSC Adv.* **8**, 24617–24626 (2018)
38. M.A. Zakria, A.A. Menazea, A.M. Mostafa, E.A. Al-Ashkar, Ultra-thin silver nanoparticles film prepared via pulsed laser deposition: synthesis, characterization, and its catalytic activity on reduction of 4-nitrophenol. *Surf. Interfaces* (2020). <https://doi.org/10.1016/j.surfin.2020.100438>
39. C.S. Ciobanu, S.L. Iconaru, F. Massuyeau, L.V. Constantin, A. Costescu, D. Predoi, Synthesis, structure, and luminescent properties of europium-doped hydroxyapatite nanocrystalline powders. *J. Nanomater.* (2012). <https://doi.org/10.1155/2012/942801>
40. S. Rahavi, A. Monshi, R. Emadi, A. Doostmohammadi, H. Akbarian, Determination of crystallite size in synthetic and natural

- hydroxyapatite: a comparison between XRD and TEM results. *Adv. Mater. Res.* **620**, 28–34 (2012)
41. B. Gayathri, N. Muthukumarasamy, D. Velauthapillai, S.B. Santhosh, V. Asokan, Magnesium incorporated hydroxyapatite nanoparticles: Preparation, characterization, antibacterial and larvicidal activity. *Arab. J. Chem.* **11**, 645–654 (2018)
 42. U. Rajaji, S. Manavalan, S.M. Chen, S. Chinnapaiyan, T.W. Chen, R.R. Jothi, Facile synthesis and characterization of erbium oxide (Er₂O₃) nanospheres embellished on reduced graphene oxide nanomatrix for trace-level detection of a hazardous pollutant causing Methemoglobinaemia. *Ultrason. Sonochem.* **56**, 422–429 (2019)
 43. M.J. Lukić, L. Veselinović, M. Stevanović, J. Nunić, G. Dražić, S. Marković et al., Hydroxyapatite nanopowders prepared in the presence of zirconium ions. *Mater. Lett.* **122**, 296–300 (2014)
 44. S. Hiromoto, M. Inoue, T. Taguchi, M. Yamane, N. Ohtsu, In vitro and in vivo biocompatibility and corrosion behaviour of a bioabsorbable magnesium alloy coated with octacalcium phosphate and hydroxyapatite. *Acta Biomater.* **11**, 520–530 (2015)
 45. A. Janković, S. Eraković, M. Mitrić, I.Z. Matić, Z.D. Juranić, G.C.P. Tsui et al., Bioactive hydroxyapatite/graphene composite coating and its corrosion stability in simulated body fluid. *J. Alloys Compd.* **624**, 148–157 (2015)
 46. M.K. Ahmed, R. Ramadan, S.I. El-dek, V. Uskoković, Complex relationship between alumina and selenium-doped carbonated hydroxyapatite as the ceramic additives to electrospun polycaprolactone scaffolds for tissue engineering applications. *J. Alloys Compd.* **801**, 70–81 (2019)
 47. O. Kaygili, S. Keser, N. Bulut, T. Ates, Characterization of Mg-containing hydroxyapatites synthesized by combustion method. *Physica B* **537**, 63–67 (2018)
 48. D. Gopi, D. Rajeswari, S. Ramya, M. Sekar, R.D. Pramod, J. Dwivedi et al., Enhanced corrosion resistance of strontium hydroxyapatite coating on electron beam treated surgical grade stainless steel. *Appl. Surf. Sci.* **286**, 83–90 (2013)
 49. K. Lin, Y. Zhou, Y. Zhou, H. Qu, F. Chen, Y. Zhu et al., Biomimetic hydroxyapatite porous microspheres with co-substituted essential trace elements: surfactant-free hydrothermal synthesis, enhanced degradation and drug release. *J. Mater. Chem.* **21**, 16558 (2011)
 50. S.F. Mansour, S.I. El-Dek, M.K. Ahmed, Physico-mechanical and morphological features of zirconia substituted hydroxyapatite nano crystals. *Sci. Rep.* **7**, 43202 (2017)
 51. V.K. Mishra, B.N. Bhattacharjee, O. Parkash, D. Kumar, S.B. Rai, Mg-doped hydroxyapatite nanoplates for biomedical applications: a surfactant assisted microwave synthesis and spectroscopic investigations. *J. Alloys Compd.* **614**, 283–288 (2014)
 52. A. Menazea, S.A. Abdelbadie, M. Ahmed, Manipulation of AgNPs coated on selenium/carbonated hydroxyapatite/ ϵ -polycaprolactone nano-fibrous via pulsed laser deposition for wound healing applications. *Appl. Surf. Sci.* **508**, 145299 (2020)
 53. H. Zhou, J. Lee, Nanoscale hydroxyapatite particles for bone tissue engineering. *Acta Biomater.* **7**, 2769–2781 (2011)
 54. K. Kaviyarasu, K. Kanimozhi, N. Matinise, C. Maria Magdalane, G.T. Mola, J. Kennedy et al., Antiproliferative effects on human lung cell lines A549 activity of cadmium selenide nanoparticles extracted from cytotoxic effects: Investigation of bio-electronic application. *Mater. Sci. Eng. C* **76**, 1012–1025 (2017)
 55. M. Wang, Y. Liu, G. Ren, W. Wang, S. Wu, J. Shen, Bioinspired carbon quantum dots for sensitive fluorescent detection of vitamin B12 in cell system. *Anal. Chim. Acta* **1032**, 154–162 (2018)
 56. S. Kumar, R. Prakash, R.J. Choudhary, D.M. Phase, Structural, XPS and magnetic studies of pulsed laser deposited Fe doped Eu₂O₃ thin film. *Mater. Res. Bull.* **70**, 392–396 (2015)
 57. H.H. Huang, C.T. Ho, T.H. Lee, T.L. Lee, K.K. Liao, F.L. Chen, Effect of surface roughness of ground titanium on initial cell adhesion. *Biomol. Eng.* **21**, 93–97 (2004)
 58. I.M. Hung, W.J. Shih, M.H. Hon, M.C. Wang, The properties of sintered calcium phosphate with [Ca]/[P] = 1.50. *Int. J. Mol. Sci.* **13**, 13569–13586 (2012)
 59. A. Toloei, V. Stoilov, D. Northwood, The relationship between surface roughness and corrosion, in *Proceedings of the ASME 2013 international mechanical engineering congress and exposition. Advanced manufacturing*, vol. 2B, (2014)
 60. M.S. Johnsson, G.H. Nancollas, The role of brushite and octacalcium phosphate in apatite formation. *Crit. Rev. Oral Biol. Med.* **3**, 61–82 (1992)
 61. A. Carino, C. Ludwig, A. Cervellino, E. Müller, A. Testino, Formation and transformation of calcium phosphate phases under biologically relevant conditions: experiments and modelling. *Acta Biomater.* **74**, 478–488 (2018)
 62. S. Sompech, A. Srion, A. Nuntiya, The effect of ultrasonic treatment on the particle size and specific surface area of LaCoO₃. *Procedia Eng.* **32**, 1012–1018 (2012)
 63. K. Kaviyarasu, A. Mariappan, K. Neyvasagam, A. Ayeshamariam, P. Pandi, R.R. Palanichamy et al., Photocatalytic performance and antimicrobial activities of HAp-TiO₂ nanocomposite thin films by sol-gel method. *Surf. Interfaces* **6**, 247–255 (2017)
 64. S. Liu, M. Hu, T.H. Zeng, R. Wu, R. Jiang, J. Wei et al., Lateral dimension-dependent antibacterial activity of graphene oxide sheets. *Langmuir* **28**, 12364–12372 (2012)
 65. K. Krishnamoorthy, M. Veerapandian, L.-H. Zhang, K. Yun, S.J. Kim, Antibacterial efficiency of graphene nanosheets against pathogenic bacteria via lipid peroxidation. *J. Phys. Chem. C* **116**, 17280–17287 (2012)

Publisher's Note Springer Nature remains neutral with regard to jurisdictional claims in published maps and institutional affiliations.